Nanoscale Advances

ROYAL SOCIETY OF CHEMISTRY

PAPER

View Article Online
View Journal | View Issue

Cite this: *Nanoscale Adv.*, 2025, **7**, 1636

Surface engineering of 3D-printed polylactic acid scaffolds with polydopamine and 4-methoxycinnamic acid–chitosan nanoparticles for bone regeneration†

Abinaya Shanmugavadivu and Nagarajan Selvamurugan *

Bone remodeling, a continuous process of resorption and formation, is essential for maintaining skeletal integrity and mineral balance. However, in cases of critical bone defects where the natural bone remodeling capacity is insufficient, medical intervention is necessary. Traditional bone grafts have limitations such as donor site morbidity and availability, driving the search for bioengineered scaffold alternatives. The choice of biomaterial is crucial in scaffold design, as it provides a substrate that supports cell adhesion, proliferation, and differentiation. Poly-lactic acid (PLA) is known for its biocompatibility and biodegradability, but its hydrophobicity hinders cell attachment and tissue regeneration. To enhance PLA's bioactivity, we fabricated 3D-printed PLA scaffolds using fused deposition modelling. They were then surface-treated with NaOH to increase their reactivity, followed by polydopamine (PDA) and 4-methoxycinnamic acid (MCA)-loaded chitosan nanoparticle (nCS) coatings though polyelectrolyte complexation. Even though MCA, a polyphenolic, is known for its therapeutic properties, its osteogenic potential is not yet known. MCA treatment in mouse mesenchymal stem cells (mMSCs) promoted increased levels of Runx2 mRNA, a key bone transcription factor. Due to MCA's hydrophobic nature, nCS were used as carriers. The PLA/PDA/nCS–MCA scaffolds exhibited exceptional compressive strength and bioactivity. Biocompatibility tests confirmed that these scaffolds were non-cytotoxic to mMSCs. Overall, this study highlights the osteogenic potential of MCA and demonstrates the improved biocompatibility, bioactivity, wettability, and cell adhesion properties of the PDA/nCS–MCA-coated PLA scaffolds, positioning it as a promising material for bone tissue regeneration.

Received 14th September 2024
Accepted 17th January 2025

DOI: 10.1039/d4na00768a

rsc.li/nanoscale-advances

1. Introduction

Bone provides structural support and contributes to motor and hematopoietic functions, and internal organ protection. It has a double-layered structure: the outer cortical bone, with 3–5% porosity, constitutes 80% of adult bone mass, while the inner cancellous bone, with 80–90% porosity, accounts for 20% of the total bone mass.[1] Bone remodeling is a continuous and dynamic process that balances bone resorption and formation, maintaining skeletal integrity and adapting to mechanical stress. This process is supported by bone's vascularized nature, enabling efficient self-repair without scarring. However, congenital or acquired bone injuries, such as those from aging and osteoporosis, can compromise bone's regenerative abilities, increasing fracture risk. In severe cases involving trauma, infections, inflammation, or tumor resection, lesions may exceed the bone's natural healing capacity, necessitating surgical intervention.[2] The limitations of autogenous, allogeneic, and xenogeneic bone grafts can be addressed through advancements in bone tissue engineering (BTE). Bioengineered bone scaffolds aim to replicate the natural properties of bone, enhancing structural support and promoting cell function, offering promising alternatives for patients with critical bone defects.[3]

In BTE, biomaterials, particularly polymers, play a crucial role in designing scaffolds that promote bone regeneration and repair. These materials serve as temporary frameworks that support cell attachment, proliferation, and differentiation, ultimately guiding the formation of new bone tissue.[4] Natural polymers, such as collagen and chitosan (CS), are often used due to their biocompatibility and ability to mimic the extracellular matrix (ECM) of bone. However, synthetic polymers like polylactic acid (PLA), polyglycolic acid (PGA), and polycaprolactone (PCL) offer greater control over degradation rates and mechanical properties, making them suitable for creating scaffolds that degrade as new bone forms. Biodegradable polymers are particularly valuable in BTE, as they allow for the

Department of Biotechnology, School of Bioengineering, SRM Institute of Science and Technology, Kattankulathur, Tamil Nadu, 603203, India. E-mail: selvamun@srmist.edu.in

† Electronic supplementary information (ESI) available. See DOI: https://doi.org/10.1039/d4na00768a

gradual transfer of load to the regenerating tissue, reducing the need for additional surgeries.[5]

PLA is a thermostable aliphatic polyester known for its biocompatibility, biodegradability, and ease of processing. Sourced from renewable materials like corn and sugarcane, PLA degrades into lactic acid, a metabolite that the body can safely eliminate, aligning with the bone regeneration timeline and minimizing long-term complications.[6] PLA scaffolds, created using techniques such as 3D printing and electrospinning, offer precise control over architecture, porosity, and mechanical properties, supporting bone growth and cell infiltration.[7] Despite their excellent mechanical strength, PLA scaffolds face limitations due to their poor bioactivity. This issue is addressed through various surface modifications, such as roughening, plasma polymerization, ion implantation, and the application of bioactive coatings.[8,9] Bioactive coatings in bone scaffolds are surface treatments that enhance scaffold performance by promoting cell attachment, proliferation, and differentiation. Various studies have coated PLA scaffolds with materials like hydroxyapatite, bioactive glass, collagen, CS, and bioactive molecules such as peptides or growth factors, all of which support better integration with bone tissue.[10]

Polydopamine (PDA) is an adhesive inspired by mussel proteins, known for forming stable coatings that enhance surface bioactivity and cell attachment on scaffolds. PDA mimics mussel-secreted proteins, which function as adhesives in wet environments due to domains rich in 3,4-dihydroxy-L-phenylalanine (DOPA) and lysine amino acids, crucial for adhesion.[11] PDA can be polymerized under alkaline conditions followed by catechol oxidation and strong substrate interactions.[12]

4-Methoxycinnamic acid (MCA) is a commonly found natural phenolic acid with a range of effects, including antibacterial, antifungal, and anti-inflammatory effects, neuroprotective properties, and cancer inhibition.[13–15] With a chemical formula of $C_{10}H_{10}O_3$ and a molecular weight of 162.19 g mol^{-1}, MCA features a cinnamic acid backbone with a methoxy group attached to the *para* position of the phenyl ring. To our knowledge, the osteogenic potential of MCA has not yet been reported, which constitutes the novelty of this study. Also, the hydrophobic nature of MCA may restrict its direct application in the human body, making biomaterial-based delivery systems necessary to enhance the bioavailability of MCA at the bone defect site.[16]

CS is a linear polysaccharide composed of randomly distributed β-(1→4)-linked D-glucosamine (deacetylated unit) and *N*-acetyl-D-glucosamine (acetylated unit). CS nanoparticles (nCS) are widely used in drug delivery systems due to their biocompatibility, biodegradability, and ability to provide controlled, sustained release of drugs. They can enhance drug stability, improve solubility, and be engineered for targeted delivery, making them a versatile option for effective therapeutic applications.[17] Also, CS has been reported to form stable coatings when PDA is used as a surface anchor forming an intermediate bridging layer between PLA and CS.[18]

The novelty of this work lies in its first-time evaluation of MCA's ability to upregulate Runx2 mRNA expression, demonstrating its osteogenic potential for BTE applications. Additionally, this study introduces an effective approach for securely anchoring nCS–MCA to 3D-printed PLA scaffolds using a mussel-inspired PDA coating, enhancing the scaffold's surface properties and ensuring the stable immobilization of nCS–MCA for sustained release and improved biomineralization.

2. Materials and methods

2.1. Materials

MCA, CS (low molecular weight, 75–85% deacetylated), sodium tripolyphosphate (TPP), MTT [3-(4,5-dimethylthiazol-2-yl)-2,5-diphenyl tetrazolium bromide], and dopamine hydrochloride were obtained from Sigma-Aldrich, St. Louis, MO, USA. The PLA [poly(lactic acid)] filament, with a thickness of 2.85 mm, was sourced from Solidspace Technology LLP, Nashik, Mumbai, India. Dulbecco's Modified Eagle's Medium (DMEM), trypsin, and phosphate-buffered saline (PBS) were purchased from Lonza, Basel, Switzerland. Fetal bovine serum (FBS) was acquired from Gibco, Gaithersburg, USA. Sodium hydroxide (NaOH), dimethyl sulfoxide (DMSO), acetic acid (AA), ethanol, and other reagents used were of analytical grade.

2.2. Methods

2.2.1. Preliminary studies to identify the osteogenic potential of MCA. Mouse mesenchymal stem cells (mMSCs; C3H10T1/2) were sourced from the National Centre for Cell Sciences (NCCS), Pune, India. The cells were cultured in DMEM with 10% FBS and a 1× antibiotic solution. Once the cells reached confluency, they were trypsinized and subcultured for further experimental procedures. mMSCs were treated with varying concentrations of MCA for 72 h. Following this, total RNA was extracted using the TRIzol method, and cDNA synthesis was carried out with an iScript cDNA synthesis kit (BioRad, Hercules, CA, USA). Quantitative polymerase chain reaction (qPCR) was performed using a QuantStudio 3 Real-Time PCR System (Life Technologies, California, USA) with SYBR Green as the detection reagent. The Runx2 forward primer sequence was CGCCTCACAAACAACCACAG (5′ to 3′) and reverse primer sequence was TCACTGTGCTGAAGAGGCTG (5′ to 3′). The relative mRNA expression levels were determined using the ΔΔCt method, with normalization to the housekeeping gene RPL13.

2.2.2. Design and fabrication of cylindrical 3D-printed PLA scaffolds. The 3D PLA scaffolds were designed using AutoCAD 2013 (Autodesk, Inc., San Rafael, CA) and exported as stereolithography (.stl) files to ensure seamless compatibility with the printing software. The PLA filament was fed into an Ultimaker 3 printer, where it was heated to 191 °C and extruded though the nozzle, resulting in a methodical, layer-by-layer construction. This process yielded cylindrical scaffolds with a diameter of 12 mm and a height of 5 mm. The scaffolds featured 0.5 mm thick strands, uniformly spaced with 0.5 mm interstitial gaps.[8,9]

2.2.3. Synthesis of MCA-loaded nCS using the ionic gelation method. nCS–MCA were synthesized utilizing the ionic gelation method. CS was initially dissolved in a 1% (v/v) AA

solution to achieve a final concentration of 0.5% (w/v). The pH of the CS solution was adjusted to 4.8 using 1 N NaOH to ensure optimal conditions for nanoparticle formation. MCA was dissolved in DMSO at varying concentrations of 10, 20, and 40 μM. The MCA solution was gradually added to the CS solution under continuous stirring to ensure uniform mixing and incorporation of MCA into the CS matrix though electrostatic interactions, hydrogen bonding, and van der Waals forces. Subsequently, a 0.2% (w/v) TPP solution was added dropwise at a rate of 0.25 mL min^{-1} to the CS–MCA mixture in a mass ratio of 4 : 1 (CS : TPP). This process was carried out with continuous stirring at 700 rpm for 1 h to facilitate the ionic cross-linking process and the formation of nCS–MCA, with the pH maintained at 4.5. The nCS–MCA suspension was centrifuged at 15 000 rpm for 40 min to separate the nanoparticles from the supernatant.[19] The supernatant containing unbound MCA was collected for subsequent quantification to calculate the entrapment efficiency. To ensure the complete removal of DMSO, the nanoparticles were washed repeatedly with a 1% trehalose solution, preserving their structural integrity. They were then centrifuged and lyophilized under vacuum at a pressure below 1 mbar and a temperature of −40 °C to eliminate any residual solvents and obtain a stable nCS–MCA powder. In parallel, blank nCS were prepared using the same ionic gelation method, but without the addition of MCA, to serve as a control in further analyses. The prepared nanoparticles, including nCS, nCS–10 μM MCA, nCS–20 μM MCA, and nCS–40 μM MCA, were analyzed using scanning electron microscopy (SEM), transmission electron microscopy (TEM), dynamic light scattering (DLS), Fourier transform infrared spectroscopy (FT-IR), and X-ray diffraction (XRD).

2.2.4. Surface engineering of 3D-printed PLA scaffolds. The 3D-printed PLA scaffolds were treated with 0.6 M NaOH for 6 h. After the alkaline treatment, the scaffolds were rinsed three times with MilliQ water, frozen overnight, and then lyophilized for 12 h. Following this, PDA was coated onto the PLA scaffolds according to previously reported studies.[12,20] Specifically, the NaOH-treated PLA scaffolds were immersed in a dopamine hydrochloride solution (2 mg mL^{-1} in 10 mM Tris buffer, pH 8.5) at 37 °C with moderate stirring for 4 h to achieve the PDA coating. Post-PDA modification, the PLA/PDA scaffolds were thoroughly rinsed with distilled water. Next, the PLA/PDA scaffolds were immersed in an nCS–MCA (10, 20, and 40 μM MCA) solution for 6 h at 37 °C. The nCS–MCA solution was prepared by suspending 5 mg mL^{-1} of nCS in a mixture of 10 mM Tris–HCl buffer and AA (v/v = 99/1). The immersion and coating process for both PDA and nCS–MCA was repeated for five cycles to ensure thorough and consistent deposition.[21] At the end of five cycles, the nCS–MCA-immobilized PLA/PDA scaffolds were washed three times with MilliQ water, frozen overnight, and lyophilized for 12 h. Concurrently, PLA/PDA/nCS scaffolds were fabricated by immersing PLA/PDA scaffolds in a blank nCS solution to serve as a control in further analyses. The prepared scaffolds, including PLA, PLA/PDA, PLA/PDA/nCS, PLA/PDA/nCS–10 μM MCA, PLA/PDA/nCS–20 μM MCA, and PLA/PDA/nCS–40 μM MCA, were subjected to a series of analyses. These included SEM, water contact angle measurements, FT-IR, and XRD analysis.

2.2.5. Scanning electron microscopy analysis. The external surface morphology and topography of the synthesized nanoparticles and scaffolds were examined using SEM (HSEM Quanta 200FEG, Netherlands). The nanoparticles were first suspended in ethanol and subjected to sonication. The resulting dispersion was then applied to a flat substrate and allowed to air-dry, forming a thin film. Prior to SEM imaging, the samples were coated with a layer of gold.

2.2.6. Transmission electron microscopy analysis. The internal structure and morphology of the synthesized nanoparticles were analysed using TEM (JEOL JEM-2100, Japan). The nanoparticles were dispersed in ethanol and sonicated to ensure a uniform suspension. A drop of the dispersion was placed onto a carbon-coated copper grid and allowed to air-dry. Prior to TEM imaging, the samples were examined at an accelerating voltage of 200 kV to capture high-resolution images of the nanoparticle morphology.

2.2.7. Dynamic light scattering analysis. The size distribution and zeta potential of the synthesized nanoparticles were analyzed using dynamic light scattering (DLS) (Malvern Zetasizer Nano ZS, UK). The nanoparticles were dispersed in deionized water and sonicated to achieve a homogeneous suspension. The dispersion was then placed in a cuvette for measurement. DLS analysis was conducted at room temperature to determine the hydrodynamic diameter and surface charge of the nanoparticles, providing insights into their size distribution and stability in a suspension.

2.2.8. X-ray diffraction analysis. XRD was performed to assess the crystalline nature of both the nanoparticles and scaffolds. The samples were then examined within the 2θ range of 5–100° at a scanning rate of 2° per min using an XPERT PRO powder diffractometer, operating at 40 kV with Cu Kα radiation. XRD patterns were recorded for various materials, including CS, TPP, MCA, PDA, PLA, nCS, PLA/PDA, PLA/PDA/nCS, PLA/PDA/nCS–10 μM MCA, PLA/PDA/nCS–20 μM MCA, and PLA/PDA/nCS–40 μM MCA.

2.2.9. Fourier-transform infrared spectroscopy analysis. FT-IR was conducted to identify functional groups and analyze the chemical interactions between components in the nanoparticles and scaffolds. The FT-IR measurements were carried out using a PerkinElmer Spectrum instrument. For FT-IR analysis, potassium bromide (KBr) pellets were prepared with a sample-to-KBr ratio of 1 : 5. The spectra were recorded in transmittance mode, scanning across a wavenumber range of 400 to 4000 cm^{-1}.

2.2.10. Water contact angle measurement. The water contact angle of each scaffold sample was measured using the water-drop method with a Phoenix 150 instrument (SEO, Seoul, Republic of Korea). This method involved carefully placing a water droplet of 5 μL volume on the surface of the scaffold, and the contact angle formed between the droplet and the scaffold surface was recorded.

2.2.11. Mechanical testing. The compressive strength of the scaffolds was evaluated using a universal testing machine (Instron 3369, USA). Each sample underwent a compressive test,

equipped with a 9.2 kN load cell, at a loading rate of 0.5 mm min^{-1} until a strain of 50% was achieved.

2.2.12. Determination of MCA entrapment efficiency. The MCA entrapment efficiency within the nCS–MCA was evaluated by analyzing the supernatant collected during nanoparticle preparation. MCA concentration in the supernatant was quantified using a UV spectrophotometer at 288 nm. Entrapment efficiency (EE) was calculated with the formula:

$$EE\% = \left[\frac{T_{mca} - F_{mca}}{T_{mca}}\right] \times 100$$

where T_{mca} is the total amount of MCA that was added and F_{mca} is the amount of unbound MCA in the supernatant.

2.2.13. *In vitro* material characterization of PLA/PDA/nCS–MCA scaffolds

2.2.13.1. In vitro biodegradation studies. The scaffolds were incubated in 1× PBS containing lysozyme at a concentration comparable to that found in circulating blood (10 000 U L^{-1}) at 37 °C. After a 28 day incubation period, the scaffolds were frozen at −80 °C overnight and then lyophilized for 12 h. The percentage of degradation was calculated using the formula:

$$\%\ \text{biodegradation} = \left[\frac{W_o - W_t}{W_o}\right] \times 100$$

where W_o represents the initial weight of the scaffold, and W_t represents the final weight post-incubation.

2.2.13.2. In vitro protein adsorption studies. Scaffolds were initially soaked in 100% ethanol for 30 min and then washed three times with MilliQ water. Following this, they were pre-wetted in 1× PBS for 90 min. After pre-wetting, the scaffolds were incubated in 3 mL of DMEM containing 10% FBS at 37 °C for 1, 6, 12, and 24 h. Upon completion of each incubation period, the scaffolds were carefully removed, blotted to remove excess moisture, and washed three times with PBS to eliminate loosely adhered proteins. The concentration of non-adsorbed proteins in the incubation solution was then measured using the Bradford assay, and the amounts of adsorbed proteins were calculated by subtracting the non-adsorbed protein from the total protein content.

2.2.13.3. In vitro compound release studies. The scaffolds were incubated in 1× PBS at 37 °C for up to 21 days to monitor MCA release. At predetermined intervals, 200 μL of the incubation medium was extracted and replaced with fresh PBS. The MCA concentration was quantified by measuring the absorbance at 288 nm, and a standard curve was used to calculate the drug concentration (20–100 μM). The cumulative release percentage was determined using the formula:

$$\text{MCA release}\% = (\text{amount of MCA released/initial concentration of MCA loaded}) \times 100$$

To confirm the presence of MCA in the release samples, high-performance liquid chromatography (HPLC) analysis was performed using an Eclipse Plus C18 column (5 μm, 4.6 × 250 mm, Agilent-1260 infinity series). The mobile phase consisted of a 70 : 30 methanol–water mixture, with a flow rate of 1.00 mL min^{-1}, and detection was carried out at 288 nm. The PBS medium, adjusted to pH 5.5, was used as the blank.

2.2.13.4. In vitro biomineralization studies. Scaffolds were immersed in 1× stimulated body fluid (SBF) and incubated at 37 °C for 7, 14, and 21 days. After each incubation period, the scaffolds were carefully extracted, rinsed three times with deionized water to remove any residual minerals, and lyophilized. The lyophilized scaffolds were then analyzed using SEM and EDS (HSEM – Quanta 200FEG, Netherlands) to assess their biomineralization and the elemental composition of the deposited apatite.

2.2.14. Sterilization and cell culture. For sterilization, the scaffolds were initially immersed in 100% ethanol for 1 h followed by incubation in 1× PBS with a 0.5× antibiotic solution (penicillin/streptomycin/amphotericin B) for 24 h. Subsequently, the scaffolds underwent UV sterilization for 30 min, with 15 min of exposure on each side. For cell seeding, the scaffolds were pre-wetted with DMEM supplemented with 10% FBS for 1 h, enhancing their surface for improved cell attachment.

2.2.15. MTT assay. mMSCs and rat primary osteoblasts were seeded onto the scaffolds at a density of 3×10^5 cells and cultured for 3 days. Following this incubation, the medium was discarded, and 200 μL of 0.05% MTT solution was introduced to each well. After a 1 h incubation at 37 °C, DMSO was added to solubilize the formazan crystals formed by viable cells. The optical density was then measured at 570 nm to assess cell viability.

2.2.16. Fluorescein diacetate staining. mMSCs were seeded on the scaffolds at a density of 3×10^5 cells and cultured for 3 days. After this incubation period, the cells were washed with 1× PBS, treated with fluorescein diacetate (FDA) solution (30 μg mL^{-1}), and then examined under a fluorescence microscope using 10× and 20× objectives.

2.2.17. Cell count and viability assays. mMSCs were seeded on the scaffolds at a density of 3×10^5 cells and cultured for 3 days. Following the incubation period, the cells were detached using trypsin, rinsed with 1× PBS, and resuspended in fresh DMEM. The cell suspension was then combined with a cell count and viability reagent and kept in the dark for 20 min. The number of cells and their viability were then evaluated using an MUSE™ cell analyzer (Millipore, USA).

2.2.18. Statistical analysis. All experiments were conducted in triplicate ($n = 3$), and data are presented as the mean ± standard deviation (SD). Statistical analysis was carried out using one-way ANOVA, with a p-value of ≤ 0.05 considered statistically significant.

3. Results

3.1. MCA stimulated Runx2 mRNA expression in mMSCs

To assess the osteogenic potential of MCA, the expression level of Runx2 mRNA in mMSCs was examined. Runx2, a master bone transcription factor, governs the differentiation of mesenchymal stem cells into osteoblastic lineage. C3H10T1/2 cells were treated with MCA at varying concentrations, ranging from 5 μM to 60 μM, for a duration of 72 h. Following

treatment, total RNA was extracted, and RT-qPCR was performed. The results demonstrated a statistically significant upregulation of Runx2 mRNA expression in 10, 20 and 40 μM MCA-treated cells compared to the control group ($p < 0.05$). Notably, the highest Runx2 mRNA expression was observed in cells treated with 20 μM MCA. Consequently, subsequent experiments focused on loading concentrations of 10, 20, and 40 μM MCA onto nCS.

3.2. Physicochemical characterisation

3.2.1. SEM, TEM and DLS analyses. The surface morphology and structural characteristics of nanoparticles and scaffolds were evaluated using SEM and TEM. SEM images of nCS and nCS–MCA revealed spherical nanoparticles with a uniform size distribution (Fig. 2A). TEM analysis provided additional details, showing well-defined spherical structures with clear boundaries, indicating high structural integrity (Fig. 2B). For the PLA-based scaffolds (PLA/PDA/nCS, and PLA/PDA/nCS–MCA), SEM images demonstrated macroporous architectures with uniformly distributed nanoparticles on the scaffold surface, highlighting the effective integration of nCS–MCA within the PLA/PDA matrix (Fig. 2C). The average pore size of the macropores in the 3D-printed scaffolds was approximately 500 μm.

The particle size, zeta potential, and polydispersity index (PDI) of nCS and nCS–MCA nanoparticles serve as critical indicators of their physicochemical properties. The zeta potential values, ranging from +38.1 to +42.3 mV, suggested strong colloidal stability (Fig. 2D). This positive charge, primarily contributed by the protonation of CS's amino groups, likely facilitates enhanced surface interactions and uniform nanoparticle dispersion in a suspension. The *Z*-average size of the nanoparticles ranged from 144.9 to 151.3 nm, with a PDI between 0.293 and 0.34, reflecting consistent nanoparticle formation and a relatively narrow size distribution (Fig. 2E). The entrapment efficiency of nCS was quantified by analyzing the MCA content in the supernatant. The results indicated that

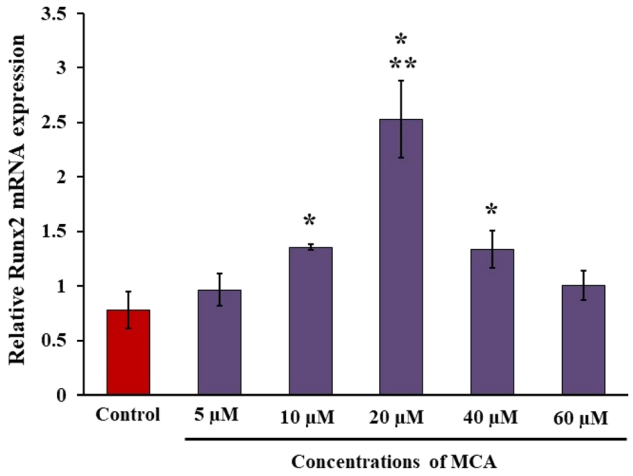

Fig. 1 Effect of MCA on osteoblast differentiation. C3H10T1/2 cells were treated with varying concentrations of MCA and cultured for 3 days. Total RNA was isolated, and RT-qPCR was performed to measure the relative mRNA levels of the osteoblast differentiation marker Runx2, normalized to RPL13A. * indicates a significant increase compared to the control ($p < 0.05$). ** indicates a significant decrease compared to all groups ($p < 0.05$).

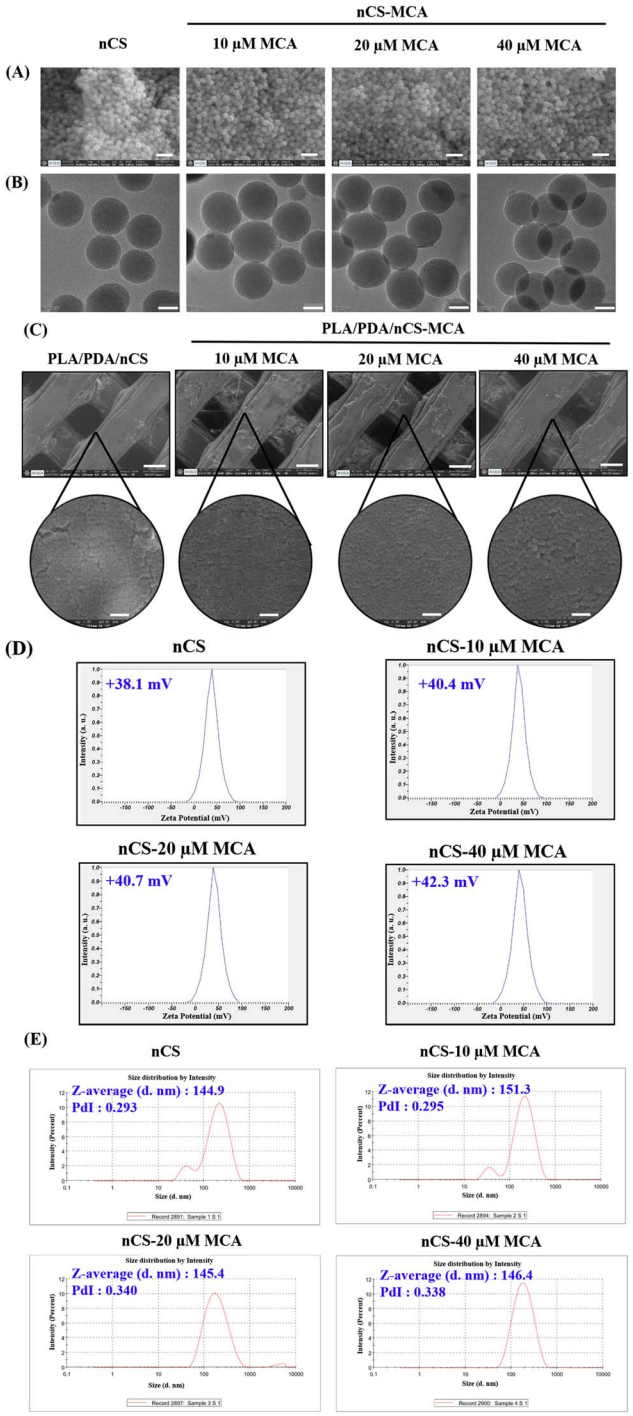

Fig. 2 (A) SEM images of nCS and nCS–MCA with a scale bar of 500 nm. (B) TEM images of nCS and nCS–MCA with a scale bar of 100 nm. (C) SEM images of the PLA/PDA/nCS and PLA/PDA/nCS–MCA scaffolds are presented, with a scale bar of 300 μm. Insets show higher magnification images of the nCS and nCS–MCA distribution on the scaffold surface, with a scale bar of 500 nm. (D and E) DLS results for nCS and nCS–MCA.

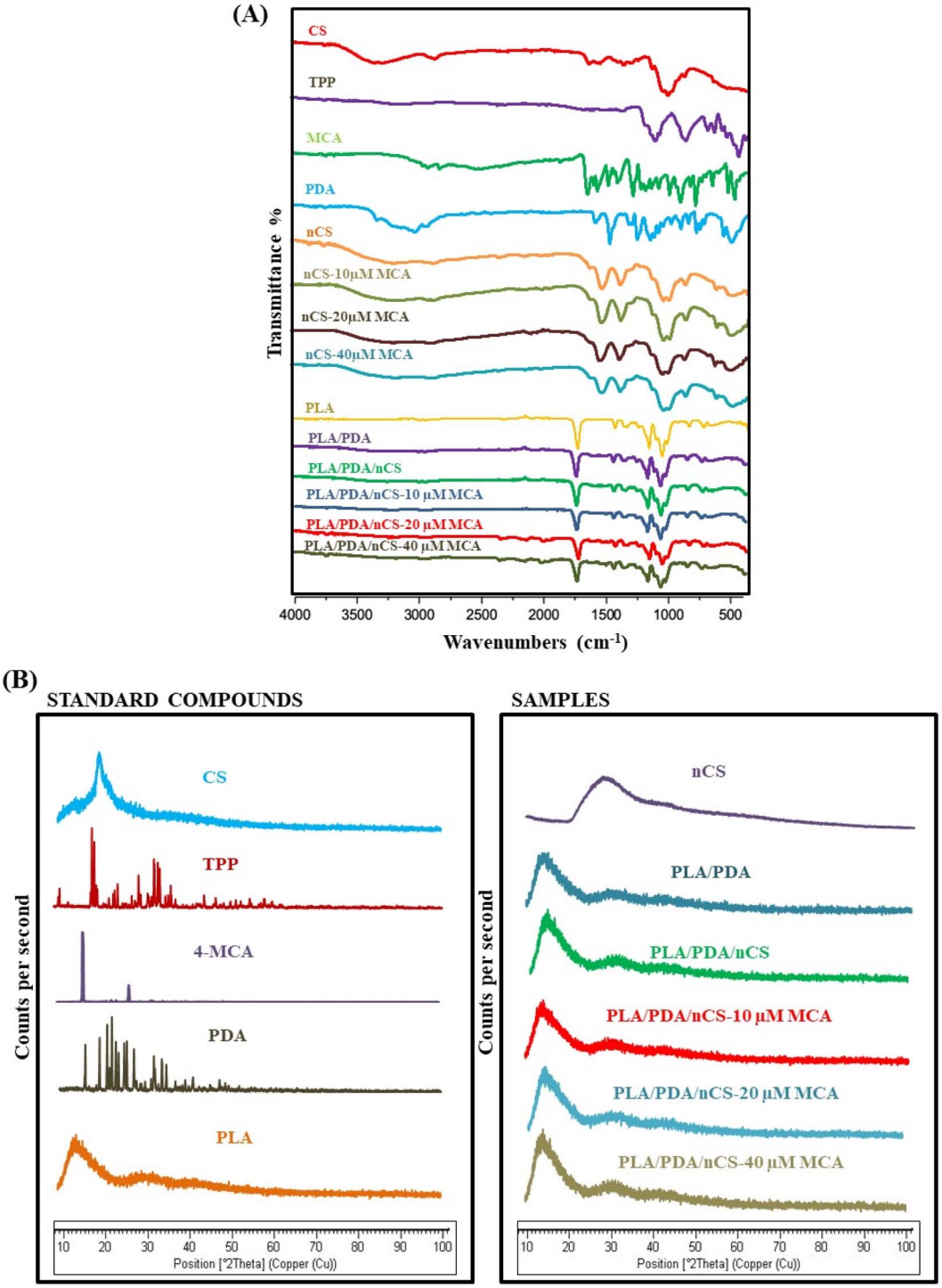

Fig. 3 (A) FT-IR spectra of CS, TPP, MCA, PDA, nCS, nCS–10 μM MCA, nCS–20 μM MCA, nCS–40 μM MCA, PLA, PLA/PDA, PLA/PDA/nCS, PLA/PDA/nCS–10 μM MCA, PLA/PDA/nCS–20 μM MCA, and PLA/PDA/nCS–40 μM MCA. (B) XRD patterns of CS, TPP, MCA, PDA, PLA, nCS, PLA/PDA, PLA/PDA/nCS, PLA/PDA/nCS–10 μM MCA, PLA/PDA/nCS–20 μM MCA, and PLA/PDA/nCS–40 μM MCA.

MCA was effectively encapsulated within nCS, with an entrapment efficiency ranging from 66.37% to 68.9%.

3.2.2. FT-IR, XRD and compressive strength analyses. FT-IR analysis was employed to identify the functional groups present in CS, TPP, PDA, PLA, and MCA, as well as to understand their chemical interactions (Fig. 3A). The FT-IR spectra of pure MCA exhibited distinct peaks at 3462 cm^{-1} and 1672.3 cm^{-1}, corresponding to O–H and C=O stretching, respectively.[22] The CS spectra showed a broad peak between 3500 and 3000 cm^{-1}, which is attributed to the stretching vibrations of the amine and OH groups in CS. The N–H stretching from amide I and II was observed at 1642 cm^{-1} and

1554 cm^{-1}, respectively.[9] For TPP, the main vibrations observed were P═O, PO_2 and PO_3 stretching at 1212 cm^{-1}, 1148 cm^{-1} and 1093 cm^{-1}, respectively; and P–O–P antisymmetric stretching at 900 cm^{-1}.[23] The PLA spectra revealed characteristic peaks at 3226.91 cm^{-1} (OH stretching), 2931.80 cm^{-1} (C–H symmetric valence vibration), and 1749.44 cm^{-1} (C═O valence vibration), with distinct peaks between 1300 and 1100 cm^{-1} corresponding to C–O–C symmetric valence vibrations.[9] The FT-IR spectra of dopamine revealed peaks at 3346 cm^{-1}, 3270 cm^{-1} and 3050.77 cm^{-1} corresponding to amine N–H, phenol O–H stretching and aromatic C═H stretching, respectively.[24] FT-IR of nCS revealed interactions between TPP and the ammonium groups in CS within the nanoparticles. The characteristic peak at 3438 cm^{-1} shifted to 3320 cm^{-1} in nCS, signifying hydrogen bonding.[19] The spectra of PLA/PDA, PLA/PDA/nCS, and PLA/PDA/nCS–MCA scaffolds exhibited distinct peaks characteristic of PLA. However, MCA-specific peaks were not observed, which could be attributed to the low concentrations of MCA utilized in the scaffolds.[8]

XRD analysis was carried out to examine the crystalline nature of the individual components and the biocomposite scaffolds (PLA/PDA, PLA/PDA/nCS and PLA/PDA/nCS–MCA). The XRD spectra of MCA exhibited sharp, intense peaks confirming its crystalline structure (Fig. 3B). The diffraction pattern of TPP and PDA also showed sharp peaks indicating their crystalline nature, whereas the diffraction patterns of nCS and PLA demonstrated semi-crystalline characteristics. The biocomposite scaffolds, PLA/PDA, PLA/PDA/nCS and PLA/PDA/nCS–MCA showed less intense peaks, indicating the semi-crystalline nature of the composites. The degree of crystallinity of the PLA/PDA/nCS scaffold was found to be 27.78%, while the PLA/PDA/nCS–MCA scaffold exhibited a crystallinity of 26.74%. The scaffolds were classified as semi-crystalline, with the inclusion of MCA having no significant effect on the crystallinity, suggesting that MCA incorporation did not alter the crystalline structure of the composite. The compressive strength analysis revealed that the PLA scaffold had a compressive strength of 77.67 MPa, while the PLA/PDA/nCS–MCA scaffold exhibited 83.85 MPa.

3.2.3. Hydrophilicity assessment of surface engineered PLA scaffolds. The water contact angle analysis revealed significant variations in hydrophilicity across the different scaffold formulations (Fig. 4). Untreated PLA displayed a contact angle of 119°, indicative of its hydrophobic nature. Following NaOH treatment, the contact angle of PLA decreased to 84°, suggesting an increase in surface hydrophilicity. A

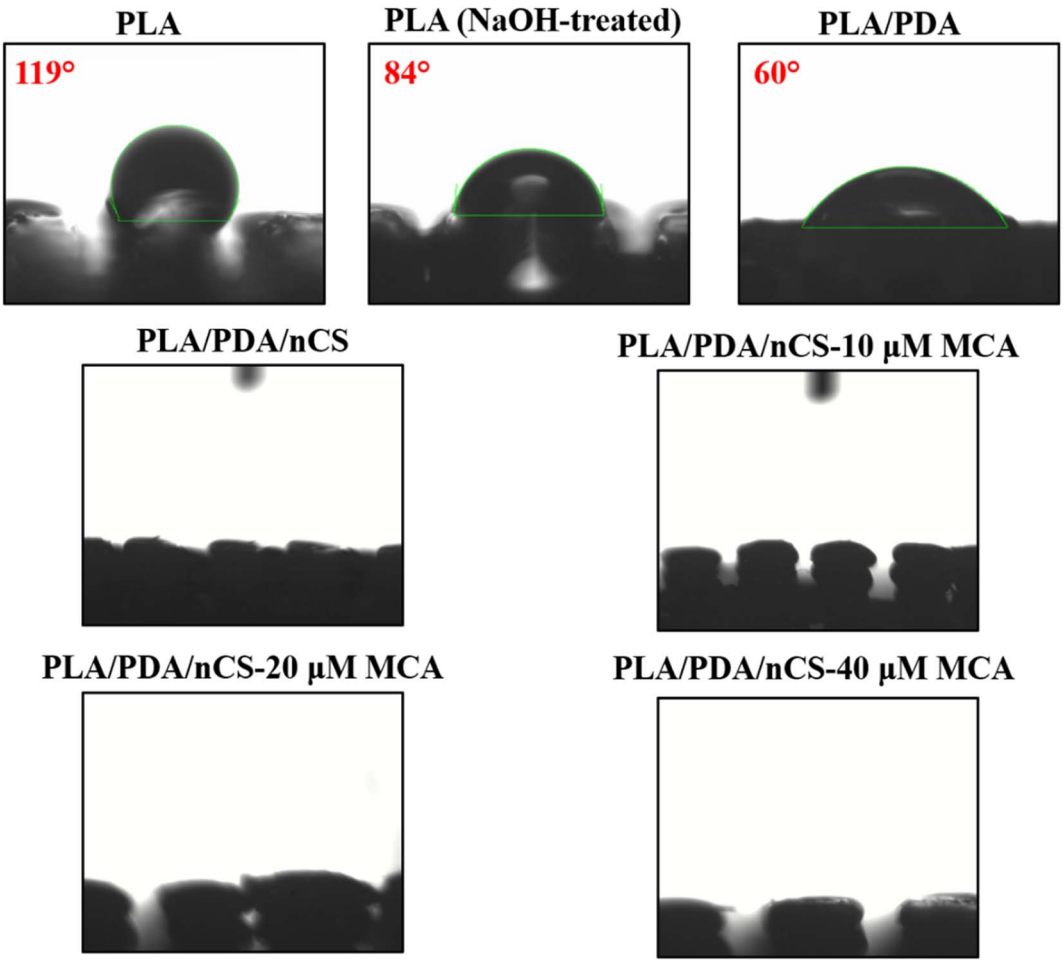

Fig. 4 Water contact angle measurement of PLA, PLA (NaOH-treated), PLA/PDA, PLA/PDA/nCS, and PLA/PDA/nCS–MCA scaffolds.

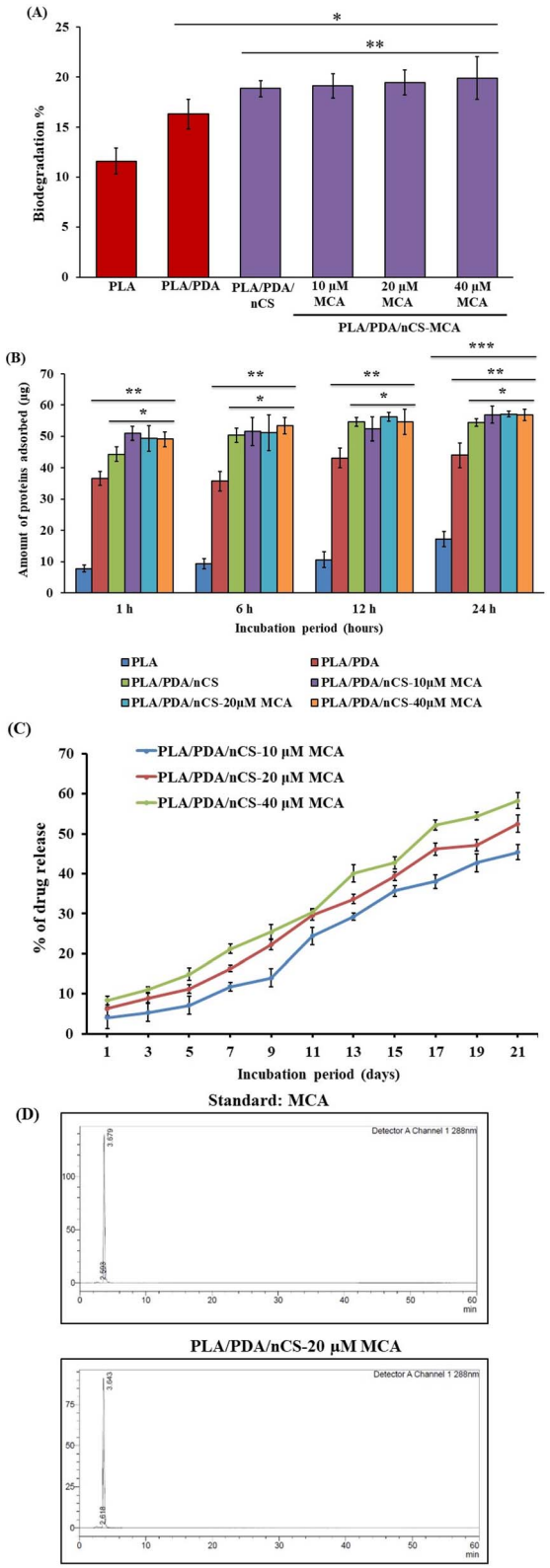

Fig. 5 Biodegradation, protein adsorption, drug release, and HPLC analysis. PLA, PLA/PDA, PLA/PDA/nCS, and PLA/PDA/nCS–MCA scaffolds were evaluated across several parameters. (A) Biodegradation rates of scaffolds in PBS containing lysozyme over 28 days. * indicates a significant increase compared to PLA ($p < 0.05$). ** indicates a significant increase compared to PLA/PDA ($p < 0.05$). (B) Protein adsorption on scaffolds at 1, 6, 12, and 24 h. * indicates a significant increase compared to the respective PLA/PDA scaffolds ($p < 0.05$). ** indicates a significant increase compared to the respective PLA ($p < 0.05$). *** indicates a significant increase compared to the respective groups at 1 h ($p < 0.05$). (C) MCA release from PLA/PDA/nCS–MCA scaffolds over 21 days. (D) HPLC chromatograms confirming the presence of MCA in the released samples, with retention times similar to the MCA standard.

further reduction in the contact angle was observed with the PLA/PDA scaffolds, which exhibited an angle of 60°, confirming enhanced hydrophilicity. Notably, the PLA/PDA/nCS and PLA/PDA/nCS–MCA scaffolds demonstrated near-zero contact angles immediately upon water-drop application, reflecting a substantial improvement in hydrophilic properties. The incorporation of MCA into the PLA/PDA/nCS scaffolds did not alter their hydrophilic characteristics, as evidenced by the maintained near-zero contact angle.

3.3. *In vitro* material characterisation

3.3.1. Biodegradation and protein adsorption studies. The degradation rate of PLA, PLA/PDA, PLA/PDA/nCS, and PLA/PDA/nCS–MCA scaffolds was evaluated after 28 days of incubation in PBS with lysozyme. The results indicated that PDA-containing scaffolds degraded significantly faster than PLA scaffolds (Fig. 5A), and PLA scaffolds with nCS exhibited an even higher degradation rate than PLA/PDA scaffolds. Protein adsorption studies revealed that PLA scaffolds coated with PDA demonstrated better protein adsorption compared to PLA alone at all time points (1, 6, 12, and 24 h). Additionally, at each time period, protein adsorption was significantly higher in the nCS and nCS–MCA coated groups compared to PLA/PDA. At 24 h, all groups showed a significant increase in protein adsorption compared to their respective values at 1 h (Fig. 5B). However, the addition of MCA had no significant effect on biodegradation or protein adsorption, suggesting that MCA did not influence these properties in the biocomposite scaffolds.

3.3.2. MCA release studies. The release profile of MCA from PLA/PDA/nCS–MCA scaffolds was tracked over a 21 day period (Fig. 5C). Unlike typical drug release profiles, no initial burst effect was observed, suggesting effective incorporation of MCA within the nCS matrix. By day 21, approximately 55% of the MCA had been released. HPLC analysis confirmed the presence of MCA, with two distinct peaks at retention times of 2.618 and 3.643 min, corresponding to its isoforms (Fig. 5D). The retention times for both standard MCA and the released MCA from the PLA/PDA/nCS–MCA scaffolds were consistent.

3.3.3. Biomineralization studies. To evaluate the potential for apatite formation, an *in vitro* biomineralization study was conducted on PLA, PLA/PDA, PLA/PDA/nCS, and PLA/PDA/nCS–MCA scaffolds. SEM analysis after 7, 14, and 21 days of incubation in SBF revealed mineralized deposits on the scaffold surfaces. At 2500× magnification, a uniform and dense deposition of apatite was observed in the nCS and nCS–MCA surface modified groups. This indicates a strong biomineralization capability (Fig. 6A). Elemental analysis though EDS detected carbon, oxygen, phosphate, and calcium within the scaffolds.

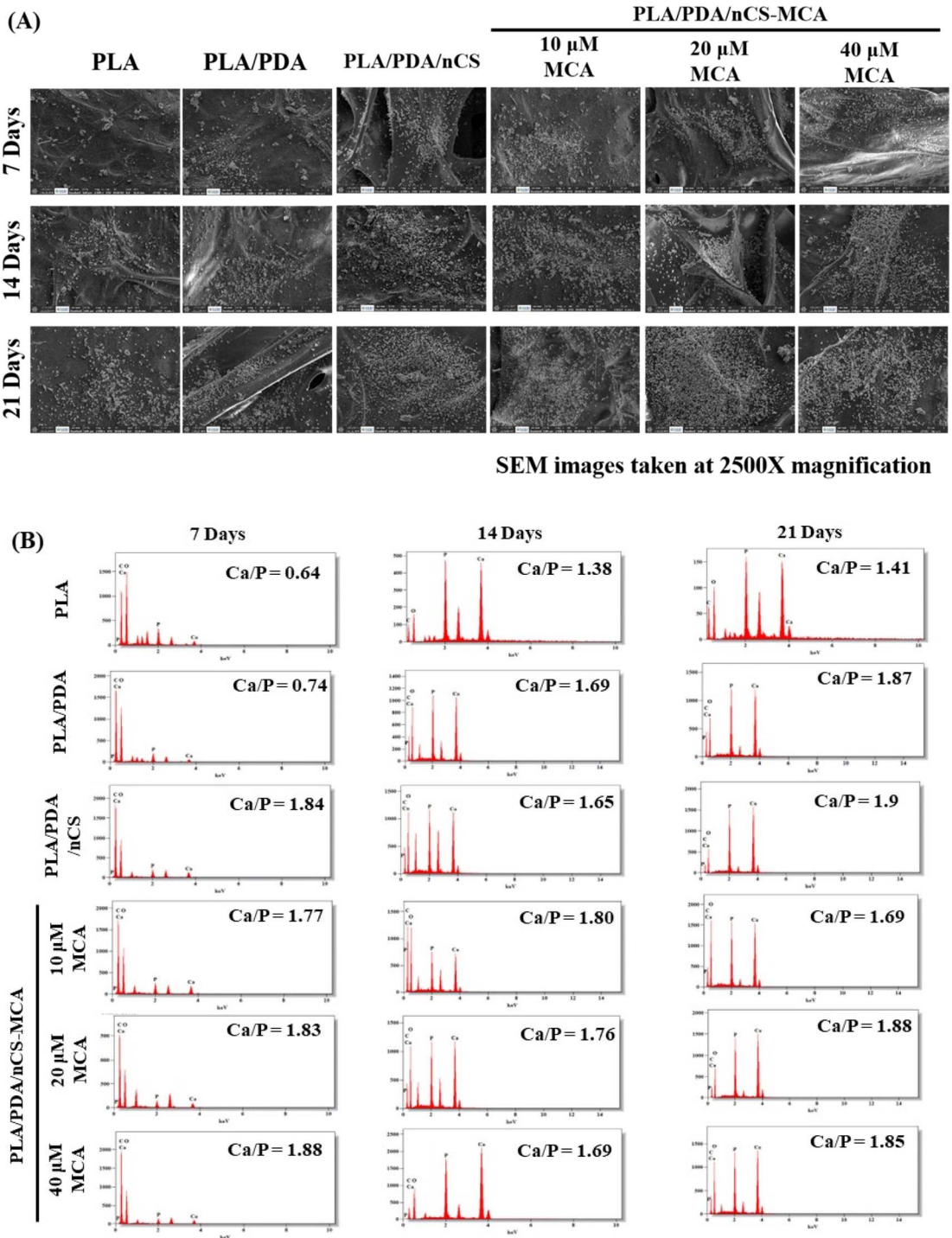

Fig. 6 PLA, PLA/PDA, PLA/PDA/nCS, and PLA/PDA/nCS–MCA scaffolds were assessed for biomineralization in SBF over 7, 14, and 21 days. (A) Mineral deposits on scaffolds observed by SEM analysis at 2500× magnification. (B) EDS spectra confirmed the presence of calcium (Ca), phosphorus (P), carbon (C), and oxygen (O) in the mineralized layers, with the corresponding Ca/P ratios.

The Ca/P ratios for the mineralized PLA scaffolds were 0.64, 1.38, and 1.41 at 7, 14, and 21 days, respectively. The PLA/PDA group initially showed a lower Ca/P ratio of 0.74 at 7 days, but extended incubation in SBF resulted in increased apatite deposition, yielding Ca/P ratios of 1.69 and 1.87 at 14 and 21 days (Fig. 6B). The nCS-modified scaffolds, including PLA/PDA/nCS and PLA/PDA/nCS–MCA, maintained Ca/P ratios between 1.6 and 1.9 across all time periods, closely matching the stoichiometric ratio of natural bone apatite. Also, qualitative SEM analysis further demonstrated a time-dependent increase in apatite formation across all scaffold groups.

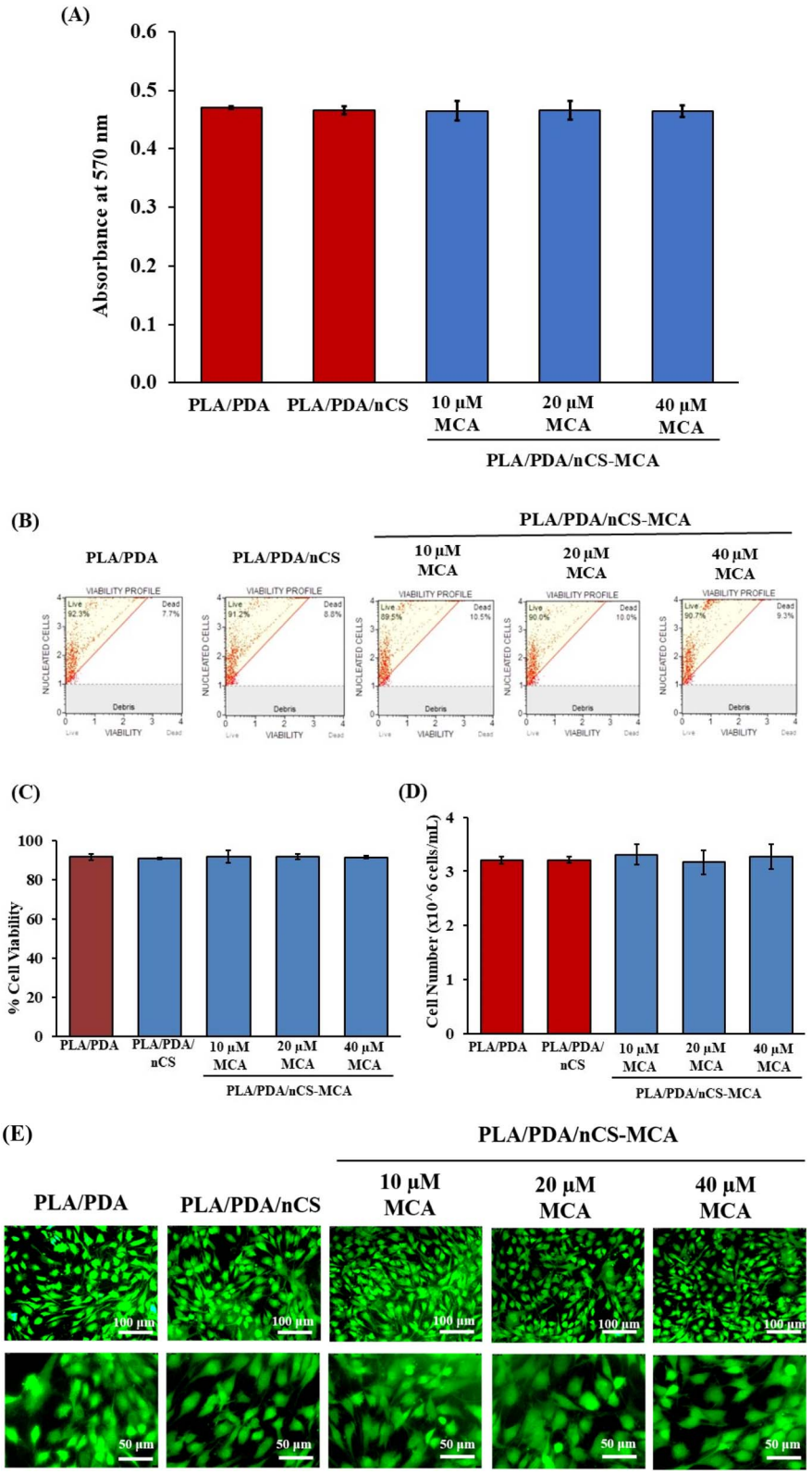

Fig. 7 Cytotoxicity and cell morphology analysis. mMSCs were seeded onto PLA/PDA, PLA/PDA/nCS, and PLA/PDA/nCS–MCA scaffolds and cultured for 72 h. (A) MTT assay. (B) The dot plots illustrate the distribution of live cells, dead cells, and cell debris, with the upper left quadrant representing viable cells and the upper right quadrant depicting dead cells. (C and D) Bar graphs showing cell viability and cell number. (E) mMSCs were stained with FDA and examined under a fluorescence microscope.

3.4. Cytotoxicity, cell viability and cell count studies

The synthesized scaffolds were assessed for cytocompatibility using the MTT assay with mMSCs (Fig. 7A). This assay evaluates cell viability by measuring the conversion of MTT into formazan crystals though mitochondrial succinate dehydrogenase activity. The results demonstrated no significant change in absorbance, indicating that the PLA/PDA, PLA/PDA/nCS, and PLA/PDA/nCS–MCA scaffolds were non-cytotoxic in mMSCs.

While the MTT assay provides insight into the metabolic activity of cells, it does not assess membrane integrity. Therefore, cell membrane integrity in response to the scaffolds was further evaluated using a Muse cell analyzer. The results showed no significant change in cell viability or cell number (Fig. 7B–D). All scaffold groups, including PLA/PDA, PLA/PDA/nCS, and PLA/PDA/nCS–MCA, exhibited similar percentages of cell viability and cell counts, indicating that both MCA and the biocomposite scaffolds were non-toxic and do not affect cell proliferation.

FDA staining revealed that mMSCs seeded on PLA/PDA, PLA/PDA/nCS, and PLA/PDA/nCS–MCA scaffolds exhibited well-extended morphology with distinct cytoplasmic extensions that support cell attachment and growth (Fig. 7E). Morphological evaluation at 20× and 40× magnification showed that the addition of MCA in the biocomposite scaffolds did not adversely affect cell morphology, indicating their non-toxic nature. Hence, these results suggested that PLA/PDA/nCS–MCA scaffolds have the potential to accelerate bone regeneration while being non-cytotoxic.

4. Discussion

BTE aims to create scaffolds that mimic the natural ECM and support bone regeneration. Advances in 3D printing, especially FDM, enable precise scaffold design, with PLA being popular due to its biocompatibility and customizable properties.[25] However, PLA lacks inherent bioactivity, necessitating surface modifications to enhance osteoconductivity. Incorporating bioactive molecules or growth factors into PLA scaffolds can also make them osteoinductive, enabling the differentiation of MSCs into osteoblasts to support bone regeneration.[26] In this work, a feasible and effective method to firmly anchor nCS–MCA onto 3D-printed PLA scaffolds though a mussel-inspired PDA coating was proposed. The nCS were loaded with MCA, a polyphenol whose osteogenic potential was evaluated. The PDA coating, serving as an intermediate bridging layer, offers abundant active sites to couple with nCS–MCA. After physicochemical characterization of the surface-engineered PLA scaffolds, their bioactivity was systematically assessed though various *in vitro* material characterization and biocompatibility studies.

MCA was selected for its potential therapeutic benefits, which are largely attributed to its chemical structure. The biological activity of phytocompounds, including MCA, is significantly influenced by their chemical structure, which impacts solubility, membrane penetration, and enzyme binding. Specifically, for cinnamic acid derivatives, bioactivity is primarily governed by the presence and positioning of hydroxy (–OH) and methoxy ($-OCH_3$) groups on the aromatic ring. The number and placement of these substituents critically define the extent and potency of their biological action. Notably, studies have demonstrated that among phenylpropanoic acids, those with the $-OCH_3$ group in the *para* position, such as MCA, exhibit pronounced hepatoprotective activity, underscoring their potential for therapeutic applications.[27] The evaluation of MCA's osteogenic potential revealed a significant increase in Runx2 mRNA expression in mMSCs, especially at 10, 20, and 40 μM concentrations, which guided the selection of these MCA-loaded nCS concentrations for further experimentation (Fig. 1). Phytocompounds have been reported to achieve peak plasma concentration within a short timeframe and are swiftly eliminated from systemic circulation.[28] Therefore, an effective delivery system is needed to prolong their bioavailability and therapeutic effects.

Nano-drug delivery systems have been employed to deliver various drugs, growth factors, and hydrophobic phytocompounds.[29,30] Natural polymers, such as CS, are especially beneficial for fabricating these nanoparticles due to their biocompatibility and effectiveness in stabilizing various phytocompounds, by enhancing their solubility and bioavailability.[19,31] Nanoparticles offer significant advantages in drug delivery, particularly in enhancing drug stability and bioavailability though controlled release mechanisms.[32] SEM and TEM analyses confirmed that both nCS and nCS–MCA nanoparticles possess a spherical morphology (Fig. 2A and B). Zhao *et al.* reported that spherical nanoparticles had better bioavailability compared to rod-shaped nanoparticles due to their uniform size and shape, which enhanced their ability to be internalized by cells, leading to better cellular uptake and more consistent drug release profiles.[33] Hejjaji *et al.* reported that a zeta potential greater than +30 mV generally indicates lower stability due to reduced electrostatic repulsion, while a zeta potential in the range of +34 to +42 mV is considered optimal for enhanced stability.[34] Accordingly, the zeta potentials of nCS and nCS–MCA, ranging from +38 to +42 mV, indicated their excellent colloidal stability (Fig. 2D). Also, the size of nCS and nCS–MCA was observed to be less than 200 nm (Fig. 2E), indicating their potential for enhanced drug release control and improved cellular interactions.[31] The entrapment efficiency of nCS–MCA nanoparticles, determined by analysing the MCA content in the supernatant, ranged from 66.37% to 68.9%. Although the direct method of preparation, which involves dispersing the drug solution in a polymeric matrix followed by the addition of a crosslinking agent, is often associated with low entrapment efficiency, this limitation was overcome by optimizing critical parameters such as polymer concentration, CS : TPP mass ratio, pH, stirring conditions, and the addition rate of TPP, as demonstrated in our previous studies.[19]

The prepared nCS and nCS–MCA were coated on the PLA/PDA scaffold *via* the immersion technique allowing the PDA to act as a natural crosslinker. Similarly, Salehi *et al.* fabricated poly(L-lactic acid) scaffolds *via* freeze-drying and coated them with nCS *via* the immersion technique.[35] The FT-IR spectra of PLA/PDA/nCS–MCA showed no new peaks, indicating no

interaction between the components.[9] Additionally, the PLA/PDA/nCS–MCA nanocomposite scaffolds maintained their semi-crystalline structure despite the inclusion of the crystalline MCA (Fig. 3).

The hydrophilicity of biomaterials is critical in influencing their interactions with biological systems, such as protein adsorption and cell attachment.[20] The surface modification techniques employed, including NaOH treatment, PDA coating and nCS incorporation, substantially improved the hydrophilicity of the scaffolds. The water contact angle measurements demonstrated a marked decrease in hydrophobicity across the modified scaffolds (Fig. 4). The nanocomposite scaffolds, PLA/PDA/nCS and PLA/PDA/nCS–MCA scaffolds exhibited near-zero contact angles, highlighting a significant enhancement in hydrophilic properties. Materials with a water contact angle between 0° and 40° are optimal for bone graft applications,[36] supporting the suitability of our PLA/PDA/nCS–MCA scaffolds for BTE applications. Consistent with SEM analysis that confirmed successful nCS–MCA incorporation on the scaffold surfaces (Fig. 2C), the reduced water contact angles further validated this integration. The mechanical strength of a scaffold is crucial for supporting cellular activities like adhesion and proliferation, which influence its overall *in vivo* performance. It also affects the scaffold's stability under physiological loads and its ability to facilitate mechanotransduction, essential for effective bone regeneration. In this study, the PLA/PDA/nCS–MCA scaffolds showed compression strength values ranging from 77.67 to 83.85 MPa, approaching those of cortical bone. The slight increase in compressive strength of the PLA/PDA/nCS–MCA scaffold can be attributed to the 5-layer coating of PDA and nCS, which enhanced the scaffold's structural integrity and strength through improved material reinforcement and interfacial bonding. The layer-by-layer assembly technique enabled the application of conformal coatings on highly porous 3D templates, effectively transferring microscale mechanical characteristics to larger-scale structures.[37]

Biodegradation is essential for BTE scaffolds, as it allows for the gradual breakdown of materials to facilitate new bone formation. Scaffolds interact with bodily fluids containing hydrolytic enzymes that accelerate their degradation. In this study, PLA/PDA/nCS and PLA/PDA/nCS–MCA scaffolds exhibited significantly higher degradation rates compared to PLA and PLA/PDA scaffolds, likely due to the increased surface area-to-volume ratio provided by nCS (Fig. 5A). nCS undergo degradation though their β-1,4-glycosidic bond cleavage and *N*-acetyl linkage hydrolysis in the presence of lysozyme, producing non-toxic oligosaccharides that integrate into ECM components.[38] PLA, on the other hand, is degraded *via* enzyme–PLA complex formation with lysozyme, which cleaves ester bonds and releases by-products.[39] Protein adsorption is critical for optimizing cellular interactions. Our findings revealed that PLA/PDA/nCS and PLA/PDA/nCS–MCA scaffolds exhibited higher protein adsorption compared to PLA and PLA/PDA (Fig. 5B). This indicates that the addition of nCS could improve scaffold performance by enhancing cellular responses and facilitating bone regeneration. A consistent and extended drug release profile is essential for bone scaffolds to ensure an effective dosage for bone tissue regeneration. Polyphenols, known for their rapid metabolism, pose a challenge for sustained delivery.[9] To overcome this, nCS were employed as a controlled release system for MCA. *In vitro* studies showed that PLA/PDA/nCS–MCA scaffolds achieve a prolonged and stable release of MCA over 21 days (Fig. 5C).

Biomineralization involves forming new bone by depositing mineral salts on a scaffold's surface when implanted and exposed to body fluids. This process promotes the accumulation of calcium phosphates, such as hydroxyapatite, which interact with the scaffold's organic polymers, enhancing mineralization and supporting bone formation.[19] Enhanced biomineralization in the PLA/PDA/nCS and PLA/PDA/nCS–MCA groups can be attributed to the initiation of nucleation sites by the polar groups in nCS (Fig. 6).

Biocompatibility is crucial for the success of biomaterial implants, influencing cell adhesion and long-term viability on the scaffold surface. In this study, the polymers used—PLA, PDA, and CS—demonstrated compatibility with diverse cell types and animal models, making them well-suited for BTE applications.[40–42] Evaluating cell attachment, morphology, and distribution on the scaffold provides essential insights into its performance and interactions with cells.[43] These characteristics were assessed though various assays, including MTT, Muse cell analysis, and FDA staining. The results confirmed that the PLA/PDA/nCS–MCA nanocomposite scaffolds are biocompatible (Fig. 7), and they do not adversely affect cell proliferation, underscoring their potential for BTE applications.

5. Conclusion

This study highlights the pivotal role of surface engineering in advancing the efficacy of 3D-printed PLA scaffolds for BTE applications. By employing surface modifications such as incorporating PDA, nCS, and MCA, we significantly enhanced the scaffolds' hydrophilicity, biomineralization, and degradation properties. Also, the biocomposite scaffolds were non-cytotoxic to mMSCs. Notably, this study is the first to reveal MCA's osteogenic potential, marking a significant advancement in scaffold development. The inclusion of MCA did not alter any of the material properties of the scaffolds and they remained non-toxic. Future investigations should focus on elucidating the cellular and molecular mechanisms underlying the osteogenic effects of these scaffolds. *In vivo* evaluations will then be crucial to further assess the scaffolds' bone regenerative potential in a physiological environment.

Data availability

The corresponding author will provide the results produced during the current investigation upon reasonable request.

Conflicts of interest

There are no conflicts to declare.

Abbreviations

AA	Acetic acid
BTE	Bone tissue engineering
CS	Chitosan
DLA	Dynamic light scattering
DMEM	Dulbecco's modified Eagle's medium
DMSO	Dimethyl sulfoxide
DOPA	3,4-Dihydroxy-L-phenylalanine
ECM	Extracellular matrix
EDS	Energy-dispersive X-ray spectroscopy
FBS	Fetal bovine serum
FDA	Fluorescein diacetate
FT-IR	Fourier transform infrared spectroscopy
HPLC	High-performance liquid chromatography
KBr	Potassium bromide
MCA	4-Methoxycinnamic acid
mMSCs	Mouse mesenchymal stem cells
MTT	3-(4,5-Dimethylthiazol-2-yl)-2,5-diphenyl tetrazolium bromide
NaOH	Sodium hydroxide
NCCS	National Centre for Cell Sciences
nCS	Chitosan nanoparticles
PBS	Phosphate-buffered saline
PCL	Polycaprolactone
PDA	Polydopamine
PGA	Polyglycolic acid
PLA	Polylactic acid
qPCR	Quantitative polymerase chain reaction
SD	Standard deviation
SEM	Scanning electron microscopy
TEM	Transmission electron microscopy
TPP	Sodium tripolyphosphate
XRD	X-ray diffraction

References

1 A. M. Parfitt, *Bone*, 2002, **30**, 807–809.
2 F. Shang, Y. Yu, S. Liu, L. Ming, Y. Zhang, Z. Zhou, J. Zhao and Y. Jin, *Bioact. Mater.*, 2021, **6**, 666–683.
3 N. Xue, X. Ding, R. Huang, R. Jiang, H. Huang, X. Pan, W. Min, J. Chen, J.-A. Duan, P. Liu and Y. Wang, *Pharmaceuticals*, 2022, **15**, 879.
4 H. Qu, H. Fu, Z. Han and Y. Sun, *RSC Adv.*, 2019, **9**, 26252–26262.
5 Z. Sheikh, S. Najeeb, Z. Khurshid, V. Verma, H. Rashid and M. Glogauer, *Materials*, 2015, **8**, 5744–5794.
6 M. A. Elsawy, K.-H. Kim, J.-W. Park and A. Deep, *Renewable Sustainable Energy Rev.*, 2017, **79**, 1346–1352.
7 S. Swetha, K. Balagangadharan, K. Lavanya and N. Selvamurugan, *Biotechnol. J.*, 2021, **16**(11), e2100282.
8 B. Ashwin, B. Abinaya, T. P. Prasith, S. V. Chandran, L. R. Yadav, M. Vairamani, S. Patil and N. Selvamurugan, *Int. J. Biol. Macromol.*, 2020, **162**, 523–532.
9 R. Bharathi, G. Harini, A. Sankaranarayanan, A. Shanmugavadivu, M. Vairamani and N. Selvamurugan, *Int. J. Biol. Macromol.*, 2023, **253**, 127492.
10 A. Dukle and M. R. Sankar, *Mater. Today Commun.*, 2024, **40**, 109776.
11 L. Jia, F. Han, H. Wang, C. Zhu, Q. Guo, J. Li, Z. Zhao, Q. Zhang, X. Zhu and B. Li, *J. Orthop. Transl.*, 2019, **17**, 82–95.
12 L. Li, Y. Li, L. Yang, F. Yu, K. Zhang, J. Jin, J. Shi, L. Zhu, H. Liang, X. Wang and Q. Jiang, *Ann. Transl. Med.*, 2019, **7**, 240.
13 Y. Wang, M. Yin, L. Gu, W. Yi, J. Lin, L. Zhang, Q. Wang, Y. Qi, W. Diao, M. Chi, H. Zheng, C. Li and G. Zhao, *Int. Immunopharmacol.*, 2023, **116**, 109782.
14 M. Rychlicka, A. Rot and A. Gliszczyńska, *Foods*, 2021, **10**, 1417.
15 S. Gunasekaran, K. Venkatachalam and N. Namasivayam, *Environ. Toxicol. Pharmacol.*, 2015, **40**, 966–974.
16 H. S. Han, S. Y. Koo and K. Y. Choi, *Bioact. Mater.*, 2022, **14**, 182–205.
17 K. Jafernik, A. Ładniak, E. Blicharska, K. Czarnek, H. Ekiert, A. E. Wiącek and A. Szopa, *Molecules*, 2023, **28**, 1963.
18 B.-B. Wang, Y.-H. Quan, Z.-M. Xu and Q. Zhao, *Prog. Org. Coat.*, 2020, **149**, 105967.
19 R. S. Leena, M. Vairamani and N. Selvamurugan, *Colloids Surf., B*, 2017, **158**, 308–318.
20 J. Park, S. J. Lee, T. G. Jung, J. H. Lee, W. D. Kim, J. Y. Lee and S. A. Park, *Colloids Surf., B*, 2021, **199**, 111528.
21 X. Ma, G. Wu, F. Dai, D. Li, H. Li, L. Zhang and H. Deng, *Carbohydr. Polym.*, 2021, **251**, 117058.
22 W. Ferenc, B. Cristóvão, J. Sarzyński and P. Sadowski, *J. Therm. Anal. Calorim.*, 2012, **110**, 739–748.
23 F. G. de Carvalho, T. C. Magalhães, N. M. Teixeira, B. L. C. Gondim, H. L. Carlo, R. L. dos Santos, A. R. de Oliveira and Â. M. L. Denadai, *Mater. Sci. Eng., C*, 2019, **104**, 109885.
24 A. Thakur, S. Ranote, D. Kumar, K. K. Bhardwaj, R. Gupta and G. S. Chauhan, *ACS Omega*, 2018, **3**, 7925–7933.
25 B. Zhang, L. Wang, P. Song, X. Pei, H. Sun, L. Wu, C. Zhou, K. Wang, Y. Fan and X. Zhang, *Mater. Des.*, 2021, **201**, 109490.
26 E. H. Baran and H. Y. Erbil, *Colloids Interfaces*, 2019, **3**, 43.
27 R. Rukkumani, K. Aruna, P. Suresh Varma and V. Padmanabhan Menon, *J. Med. Food*, 2004, **7**, 456–461.
28 S. N. B. Selby-Pham, R. B. Miller, K. Howell, F. Dunshea and L. E. Bennett, *Sci. Rep.*, 2017, **7**, 1931.
29 M. J. Mitchell, M. M. Billingsley, R. M. Haley, M. E. Wechsler, N. A. Peppas and R. Langer, *Nat. Rev. Drug Discovery*, 2021, **20**, 101–124.
30 N. T. Vittala Murthy, S. K. Paul, H. Chauhan and S. Singh, *Curr. Drug Delivery*, 2022, **19**, 182–191.
31 K. Balagangadharan, R. Trivedi, M. Vairamani and N. Selvamurugan, *Carbohydr. Polym.*, 2019, **216**, 1–16.
32 S. Shen, Y. Wu, Y. Liu and D. Wu, *Int. J. Nanomed.*, 2017, **12**, 4085–4109.
33 Y. Zhao, Y. Wang, F. Ran, Y. Cui, C. Liu, Q. Zhao, Y. Gao, D. Wang and S. Wang, *Sci. Rep.*, 2017, **7**, 4131.

34 E. M. A. Hejjaji, A. M. Smith and G. A. Morris, *Int. J. Biol. Macromol.*, 2018, **120**, 1610–1617.
35 M. Salehi, M. Naseri-Nosar, M. Azami, S. J. Nodooshan and J. Arish, *Tissue Eng. Regener. Med.*, 2016, **13**, 498–506.
36 N. G. Rim, S. J. Kim, Y. M. Shin, I. Jun, D. W. Lim, J. H. Park and H. Shin, *Colloids Surf., B*, 2012, **91**, 189–197.
37 X. Liu, C. Zhou, Q. Xie, L. Xia, L. Liu, W. Bao, H. Lin, X. Xiong, H. Zhang, Z. Zheng, J. Zhao, W. Liang and J. Transl, *Med*, 2024, **22**, 1001.
38 E. Szymańska and K. Winnicka, *Mar. Drugs*, 2015, **13**, 1819–1846.
39 S. Farah, D. G. Anderson and R. Langer, *Adv. Drug Delivery Rev.*, 2016, **107**, 367–392.
40 K. Peng, S. Chen, V. Senthooran, X. Hu, Y. Qi, C. Zhang, L. Wu and J. Wang, *Int. J. Biol. Macromol.*, 2024, **279**, 135055.
41 J. Miszuk, J. Hu, Z. Wang, O. Onyilagha, H. Younes, C. Hill, A. V. Tivanski, Z. Zhu and H. Sun, *J. Biomed. Mater. Res., Part B*, 2024, **112**(8), e35456.
42 W. Tang, P. Pan, T. Chen, J. Wang, X. Cui, W. Liu and L. Kan, *Colloids Surf., B*, 2025, **245**, 114199.
43 S. Mohammadi, F. Ghasemi, S. A. Alavi G. and E. Alemzadeh, *Tissue Cell*, 2024, **91**, 102536.